PHYSICAL REVIEW LETTERS

Ponderomotive Electron Acceleration in a Silicon-Based Nanoplasmonic Waveguide

S. Sederberg[*] and A. Y. Elezzabi

Ultrafast Optics and Nanophotonics Research Laboratory, University of Alberta, Edmonton, Alberta T6G 2V4, Canada

Ponderomotive electron acceleration is demonstrated in a semiconductor-loaded nanoplasmonic waveguide. Photogenerated free carriers are accelerated by the tightly confined nanoplasmonic fields and reach energies exceeding the threshold for impact ionization. Broadband ($375 \text{ nm} \leq \lambda \leq 650 \text{ nm}$) white light emission is observed from the nanoplasmonic waveguides. Exponential growth of visible light emission confirms the exponential growth of the electron population, demonstrating the presence of an optical-field-driven electron avalanche. Electron sweeping dynamics are visualized using pump-probe measurements, and a sweeping time of 1.98 ± 0.40 ps is measured. These findings offer a means to harness the potential of the emerging field of ultrafast nonlinear nanoplasmonics.

The interaction of intense laser pulses with solids reveals fundamental insight into highly nonlinear optical processes and their potential utility for future optical information processing technology. To date, most investigations involve liberating charge carriers and observing their subsequent interaction with either the solid or its surrounding medium. In analogy to extreme nonlinear interactions in gases, electrons can be freed through either multiphoton or tunneling ionization, where the dominant process is determined by the laser photon energy, the electric field strength, and the electronic band gap energy of the material [1]. When investigating extreme nonlinearities in solids, parameters that favor tunneling ionization are favorable, as the multiphoton absorption regime exhibits a lower electric field damage threshold.

The high density and atomic periodicity of crystalline solids provides the potential for efficient high-harmonic generation with greater cutoff energies [2]. Intense terahertz fields have been used to drive electron-hole pairs to undergo dynamical Bloch oscillations in a semiconductor, generating high harmonics spanning terahertz to visible frequencies [3]. Femtosecond ~1.5-cycle light pulses have also been used to transform electrically insulating silica to a conductive state on a femtosecond time scale and this effect has enabled absolute carrier-envelope phase measurements of light pulses in a solid-state device [4,5].

In the case when electrons are liberated on the surface of a metal film, they can be ponderomotively accelerated to ~keV energies by surface plasmon (SP) fields in the adjacent vacuum region [6]. Surface plasmons excited on metallic nanofilms and nanostructures provide a combination of a high electric field gradient and electric field enhancement, key factors for strong ponderomotive electron acceleration (PEA) [7]. Plasmon-based PEA has been demonstrated in several configurations, including thin films [6–10] and various nanostructures [11–13]. In each of these investigations, electrons were emitted from a metal and

accelerated in the adjacent vacuum. Although this enables accurate characterization of the electron energy spectrum, power scaling, and carrier-envelope phase dependency, there is no physical restriction precluding plasmon-based PEA in a solid-state medium (i.e., nonvacuum).

Nanoplasmonic waveguides have tightly confined field mode profiles [14] that make them ideal for PEA in an integrated chip-scale system. An interesting situation arises when the nanoplasmonic waveguide is loaded with a material, such as a semiconductor. In this scenario, photoexcited electrons in the semiconductor are free to interact with the plasmonic fields in the same manner as in free space. The primary difference lies in the electron interaction with the semiconductor. For instance, the effective electron mass depends on the semiconductor band structure. Moreover, as electrons are accelerated in a semiconductor, they undergo collisions with valence band (VB) electrons within a spatial distance given by the mean free path. A semiconductor-loaded nanoplasmonic waveguide also opens new avenues for electron injection. Depending on the semiconductor band gap energy and photon energy, free carriers can be excited by linear absorption or two-photon absorption (TPA), which are more efficient than multiphoton or tunneling ionization in the metal.

In this Letter, we demonstrate PEA in a solid for the first time, in a semiconductor-loaded nanoplasmonic waveguide. Photoexcited electrons are ponderomotively accelerated in the steep field gradient at the semiconductor-metal interface, driving an electron avalanche. Broadband ($375 \text{ nm} \leq \lambda \leq 650 \text{ nm}$) white light emission from the waveguide is observed, signifying collisions between ponderomotively accelerated electrons and VB electrons. Exponential growth of the white light power with the laser power confirms a new strong-field phenomenon of ponderomotive-force-driven electron avalanche multiplication. Pump-probe experiments reveal that the ponderomotive force sweeps free carriers away from the probed region on a

1.98 ± 0.40 ps time scale, demonstrating the potential for ultrafast nanoplasmonic modulators, avalanche photodetectors, and electronic-plasmonic transducers. This nanoplasmonic structure is compatible with electronics and photonics technologies and has an ultracompact footprint area of $0.43 \ \mu m^2$.

Indispensable in the electronics industry, silicon (Si) has also been used for sophisticated integrated photonics and nanoplasmonics circuitry [15,16]. With a high refractive index of $n = 3.48$ at $\lambda = 1.55 \ \mu m$, Si-loaded nanoplasmonic waveguides enable tight mode confinement to the metal-Si interfaces. Figure 1(a) shows the highly asymmetric mode profile that is calculated for a subwavelength Si core with a width $w = 100$ nm and height $h = 340$ nm, and capped with a $t = 60$ nm thick gold (Au) film. The electric fields are tightly confined to the Au-Si interface and decay with a characteristic length $\alpha_0 = 135$ nm ($\lambda/11.5$), making this structure attractive for PEA. Additionally, Si has a high TPA coefficient $\beta_{TPA} = 0.68$ cm/GW at $\lambda = 1.55 \ \mu m$ [17], opening the possibility for a large ($\sim 10^{19}$–10^{20} cm^{-3}) photoinjected electron population to interact with the plasmonic fields.

A rigorous treatment of the time dynamics of PEA in a semiconductor would require solution of the nonequilibrium Boltzmann transport equation, electromagnetic fields in the nanoplasmonic waveguide, and silicon band structure dynamics. Here, we focus on estimating the energies attained by ballistic electrons before undergoing their first collision (i.e., their first 28 nm of motion [18–20]), providing insight into the nature of their first collision and subsequent interactions.

Electron trajectories are calculated in two steps. First, time-varying fields of a $\tau_p = 84$ fs pulse propagating through the nanoplasmonic waveguide are obtained via finite-difference time-domain (FDTD) simulations [21]. A snapshot of the E_y electric field component is shown in Fig. 1(b). Because of the tight confinement of electromagnetic energy to the Si-Au interface, Ohmic losses limit the propagation distance of this mode to $L_{prop} = 3.1 \ \mu m$. Next, the electron trajectories are calculated from the time-varying electromagnetic fields. Electrons are released into the waveguide at random locations and times during the

simulation. Each electron is given a randomly oriented initial kinetic energy $KE = 2h\nu - E_g = 0.5$ eV, where h is Planck's constant, ν is the photon frequency, and $E_g = 1.1$ eV is the Si band gap energy. The electron trajectories are calculated by integrating the classical equation of motion for an electron in an electric field,

$$v(t) = v_i(t_0) + \int_{t_0}^{t} \frac{eE_{SP}(t)}{m_e^*} dt,$$

where $v(t)$ is the electron velocity, t_0 is the time of electron excitation via TPA, $v_i(t_0)$ is the initial electron velocity, e is the elementary charge, $m_e^* = 0.26 m_0 = 2.37 \times 10^{-31}$ kg is the electron effective mass in Si [19], and $E_{SP}(t)$ is the electric field experienced by the electron during its trajectory. Since the electron acceleration dynamics occur on a much faster time scale (<100 fs) than electron thermalization ($\sim$ps), m_e^* can be assumed constant during the acceleration dynamics. Electrons that collide with the Au or waveguide sidewalls are eliminated from the simulation, as they may recombine or be emitted from the Si (depending on their energy).

Simulations are performed for three electric field strengths, $E_{SP} = 1$, 3, and 5 V/nm. Twenty-one trajectories of electrons injected at different points in time for $E_{SP} = 3$ V/nm are shown in Fig. 2(a), and are analogous to those calculated for PEA in free space [7]. Most electrons are accelerated in the directions of highest electric field gradient, normal to the Au-Si interface. The cycle-by-cycle electron acceleration is clearly visible from the "quiver" of the electron trajectories.

The rate of electron photoexcitation by the E_{SP} field is given by

$$\frac{dN(\vec{r}, t)}{dt} = \frac{\beta_{TPA}}{2h\nu} I_{SP}^2(\vec{r}, t),$$

where $N(\vec{r}, t)$ and $I_{SP}^2(\vec{r}, t)$ are the instantaneous, local electron density and electromagnetic intensity, respectively [22]. Each electron is assigned a weighting factor proportional to $I_{SP}^2(\vec{r}, t)$ at its injection coordinates to account for the spatiotemporal variation of N. The average velocity during the first 28 nm of each electron's trajectory is calculated, and spectra of the average electron energies
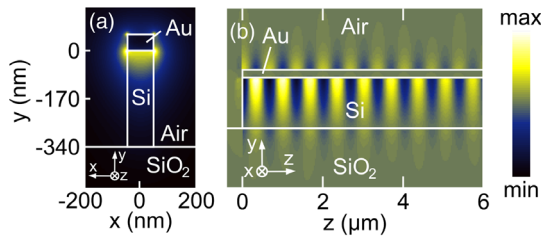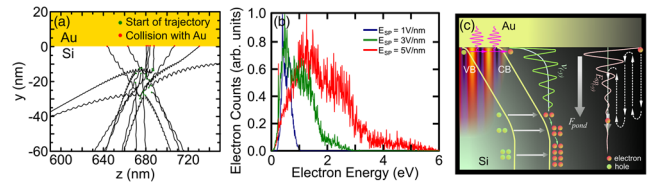

FIG. 1 (color online). (a) Mode intensity distribution in a $w \times h = 100 \times 340$ nm Si-loaded nanoplasmonic waveguide for $\lambda = 1550$ nm. (b) Time snapshot of electric field at $\lambda = 1550$ nm propagating through the nanoplasmonic waveguide.

FIG. 2 (color online). (a) Calculated trajectories of 21 electrons. (b) Calculated electron energy spectra for $E_{SP} = 1$, 3, and 5 V/nm. (c) Schematic depiction of relevant physical processes: E_{SP} field propagation, TPA, PEA, and avalanche multiplication.

before their first collision are compiled, as shown in Fig. 2(b). These spectra are analogous to those reported previously for plasmonic structures [6–13].

For modest electric fields of $E_{SP} = 3$ V/nm, electrons are accelerated to 3 eV, and for $E_{SP} = 5$ V/nm, they exceed energies of 5 eV. Interestingly, electrons are easily accelerated above the threshold energy for impact ionization in Si, $E_t = 2.3$ eV [23]. Impact ionization is a three-particle process that can be observed in Si when TPA-generated electrons interact with a strong electric field. After acceleration, they undergo collisions with bound electrons in the Si VB. Conduction band electrons with energies above E_t excite a new electron-hole (e-h) pair. Secondary e-h pairs can gain energy in the same manner and proceed to multiply in an "avalanche mode," yielding exponential growth of the electron population. These results signify that the experimental conditions required to observe a PEA-driven electron avalanche in a Si-loaded nanoplasmonic waveguide are met with standard ultrafast laser pulse excitation.

Figure 2(c) outlines this phenomenon. As femtosecond pulses propagate through the waveguide, free carriers are excited via TPA. They then accelerate ballistically in the plasmonic field before their first collision (∼28 nm). Electrons with energies less than E_t at their first collision can emit a photon, depending on the nature of the collision. Electrons with energies greater than E_t generate new e-h pairs, and return to the conduction band edge. The new e-h pairs also accelerate in the plasmonic field and can initiate impact ionization, resulting in the avalanche growth of free carriers.

Direct insight into electron avalanche multiplication and collisional dynamics has previously been gained by careful analysis of light emission from a variety of Si electronic devices under high reverse-bias voltage, including diodes and transistors [24–26]. For sufficient voltage, an electron avalanche is created and light emission (spanning visible to near-infrared wavelengths) arising from electron collisions is easily observed.

Two signatures from PEA in Si-loaded nanoplasmonic waveguides are apparent: (1) light emission signals arising from electron collisions, and (2) measurement of electron time-dynamics in the waveguide. In both cases, it is crucial to directly excite the input facet of the waveguide and measure signals from its output facet, without assistance from an on-chip coupler. Therefore, we collinearly end-fire couple $\lambda = 1.55$ μm femtosecond pulses ($\tau_p = 84$ fs) into the Si-based nanoplasmonic waveguide and outcouple signals in the same manner. To achieve collinear coupling in very short $L \leq 10$ μm waveguides, the substrate surrounding a set of waveguides with different lengths is etched to a depth of 75 μm, and one end-facet is cleaved off, as shown schematically in Fig. 3(a). This enables direct excitation of the waveguide with a microscope objective, and outcoupling of transmitted signals with a single-mode
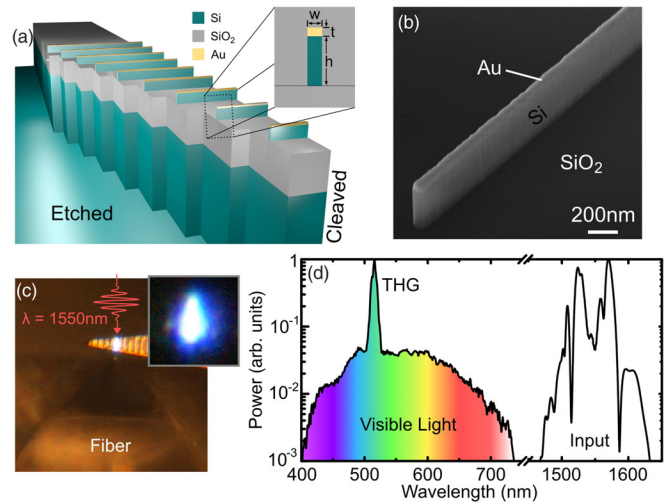

FIG. 3 (color online). (a) Schematic of nanoplasmonic waveguides situated on an etched ridge. (b) SEM of a single nanoplasmonic waveguide. (c) Top-view microscope image of experimental configuration and visible light emission from a nanoplasmonic waveguide. (d) Spectra of the transmitted laser pulses and visible light emission.

fiber. A scanning electron micrograph (SEM) of an individual Si-based nanoplasmonic waveguide is shown in Fig. 3(b). Cross-sectional dimensions of the Si core are measured to be $w \times h = 95 \times 340$ nm and the Au cap has a thickness $t = 60$ nm. The cut-back method was used to determine the linear propagation losses of the nanoplasmonic waveguides, and a propagation length of $L_{prop} = 2.0$ μm was measured.

For peak input powers above $P_{peak}^{\omega} = 10$ W, bright visible light emission is observed from the waveguides under normal room lighting. Scattered visible emission collected from above the sample by a microscope objective and delivered to a camera is shown in Fig. 3(c). Visible light emitted from the output facet of the waveguide was coupled to a single-mode fiber and delivered to a spectrometer. The transmitted laser pulse spectrum is shown together with the visible emission spectrum in Fig. 3(d). The visible emission consists of a third-harmonic (TH) signal that spans 500 nm $\leq \lambda \leq$ 530 nm and a broad white light background spanning 375 nm $\leq \lambda \leq$ 650 nm (1.9 eV $\leq h\nu \leq$ 3.3 eV). Depending on alignment, wavelengths exceeding $\lambda = 725$ nm were observed. TH signals have previously been observed from plasmonic structures [27] and do not directly relate to this study of PEA. Rotation of the excitation polarization reveals that the white light power is maximized when the transverse magnetic E_{SP} mode is excited in the nanoplasmonic waveguide. The absence of distinct atomic emission lines, the lack of damage at the input facet, and the observation of monotonically increasing visible light power with input power P_{in}^{ω} confirm that surface breakdown does not occur.

As the laser pulses propagate through the nanoplasmonic waveguide, electrons are excited via TPA from the VB into the indirect band gap ($E_g = 1.1$ eV) at the conduction band (CB) X valley. The average excess energy per electron is 0.5 eV and the electron energy distribution lies near the bottom of the indirect CB edge. Since the energy of the white light spectrum (1.9 eV $\leq h\nu \leq 3.3$ eV) is much higher than $E = 2h\nu$, the electrons must acquire energy and climb high into the CB. Since electrons with energies greater than $E_{tot} = E_t + E_g \sim 3.4$ eV initiate impact ionization, a photon cutoff energy of 3.4 eV is expected. This agrees well with the measured value of 3.3 eV.

To describe our observations theoretically, we calculate the emission spectrum using a multimechanism model for photon generation by Si junctions in avalanche conditions [28] (details are provided in the Supplemental Material [29]). Three emission mechanisms are used in this model: (1) direct interband recombination between hot e-h pairs near $k = 0$, (2) intraband transitions, and (3) indirect interband recombination of e-h pairs. Figure 4(a) illustrates the model applied to the experimental data. The excellent agreement between the model and experiment demonstrates that the white light emission originates from an electron avalanche in the Si. Although electron avalanche multiplication and light emission have previously been observed in Au nanowire arrays, this model confirms that the light emission originates from the Si [50]. Furthermore, the time dynamics of the observed process are much faster than multiphoton luminescence in Au, as discussed later.
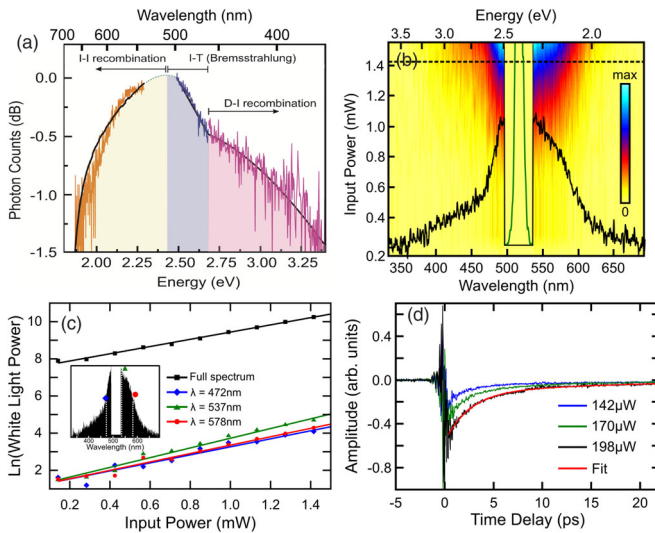

FIG. 4 (color online). (a) Experimentally measured photon counts versus photon energy, along with curves fitted with a multimechanism model. (b) Surface plot of white light spectrum versus P_{in}^{ω}. The black spectrum is measured at $P_{in}^{\omega} = 1.42$ mW and the green curve depicts the TH spectrum (removed for clarity). (c) Measured white light counts (natural logarithmic scale) versus P_{in}^{ω} for the total spectrum and individual wavelengths $\lambda = 472$, 537, and 578 nm. (d) Time-dependent power transmission for cross-polarized pump-probe measurements.

A surface plot showing the white light spectrum versus P_{in}^{ω} is displayed in Fig. 4(b). Through FDTD simulations, the peak electric field in the nanoplasmonic waveguide is calculated to be systematically varied between $0.9 \leq |E_{SP}| \leq 4.8$ V/nm, which matches the simulation conditions presented earlier. The overlay depicts the white light spectrum obtained for $P_{peak}^{\omega} = 165 \pm 3$ W measured at the output facet of the nanoplasmonic waveguide, where the TH spectral contributions are removed for clarity. A signature of the avalanche process would be the exponential growth of the electron population or equivalently, the exponential growth of light emission with P_{in}^{ω}. Figure 4(c) shows the power scaling of the total white light power P_{wh} (plotted on a natural logarithmic axis), which grows exponentially according to the relation $P_{wh} \propto \exp(\gamma P_{in}^{\omega})$, where $\gamma = 2.38 \pm 0.15$ mW^{-1}. Exponential growth is observed at all wavelengths within the spectrum, as shown for $\lambda = \{472, 537, 578\}$ nm in Fig. 4(c). The distinct exponential growth signifies that impact ionization and avalanche multiplication have taken place due to PEA.

Additional evidence signifying PEA-driven avalanche multiplication is revealed through temporal electron dynamics. Electrons are generated in the Si waveguide core via TPA, and most of them are injected close to the Au-Si interface, where the intensity is greatest. In the presence of a strong ponderomotive force F_{pond}, electrons in the Si are accelerated and quickly swept away in the E_{SP} field (~ 1 V/nm). After several collisions, the electrons travel at the saturation velocity $v_s \approx 1.3 \times 10^5$ m/s [20]. Thus, within ~ 1.0 ps, electrons traverse $\alpha_0 = 135$ nm from the Au-Si interface, and within ~ 2.6 ps they cross the entire Si core ($h = 340$ nm). Therefore, the measured electron dynamics should take place on this time scale.

Ultrafast pump-probe experiments are performed on the nanoplasmonic waveguides to investigate TPA and free-carrier absorption, and to visualize the electron sweeping dynamics. Cross-polarized pump-probe experiments (x-polarized pump, y-polarized probe) enable pump filtering with a polarizer, providing precise details of the time-dynamic nonlinear interaction. Time-domain traces for pulses propagated through a nanoplasmonic waveguide for varying pump power $P_{in}^{\omega} = \{142, 160, 198\} \pm 28$ μW are shown in Fig. 4(d). Interference fringes appear as the pulses begin to overlap, and arise from the mixed polarization components at the microscope objective focus and the mixed polarization components of the highly confined nanoplasmonic mode profile. As the pulse peaks coincide, TPA and free-carrier absorption produce a sharp drop in power transmission. The electron avalanche multiplies N, enabling distinct signal modulation at low P_{in}^{ω}. As N decreases due to field sweeping and recombination (two body, surface, Auger), the transmitted signal recovers to its original amplitude. This occurs on two time scales: $\tau_1 = 1.98 \pm 0.40$ ps and $\tau_2 = 17.9 \pm 6.8$ ps, which are much faster than what is typically observed in a Si-photonic

waveguide. Similar measurements performed on bare Si waveguides reveal a $\tau = 265$ ps recombination time [51].

The τ_1 time scale is in excellent agreement with the expected sweeping time (~1.0–2.6 ps) required for electrons to travel ~135–340 nm away from the Au-Si interface to a region where they no longer interact with the probe. The τ_2 time scale is attributed to the free-carrier lifetime in Si. Reduction of the free-carrier lifetime to $\tau_2 = 17.9 \pm 6.8$ ps in silicon waveguides typically requires ion implantation or carrier sweeping with a diode [52,53]. In the present case, Au diffusion into the Si waveguide core increases the density of recombination centers and surface traps near the Si-Au interface, increasing the surface recombination velocity.

In summary, these experiments demonstrate the first observation of ultrafast plasmon-based PEA in a semiconductor. Energetic electron collisions with valence electrons drive impact ionization, multiplying the electrons in an avalanche manner. This interaction manifests itself through strong broadband white light emission, which grows exponentially with input power, and ultrafast electron sweeping. Ultrafast electron sweeping is visualized using pump-probe time-domain spectroscopy. These measurements are performed in a structure that is compatible with electronics, photonics, and plasmonics technologies, and occupies a footprint of 0.43 μm^2. The sensitive avalanche process will enable efficient ultrafast nanoplasmonic circuitry and plasmonic-electronic interfacing. These investigations open the door for ultrafast plasmon-based PEA in semiconductors.

[*]Present address: Max-Planck-Institute of Quantum Optics, Hans-Kopfermann-Strasse 1, 85748 Garching, Germany.

[1] L. V. Keldysh, J. Exp. Theor. Phys. **20**, 1307 (1965).

[2] S. Ghimire, A. D. DiChiara, E. Sistrunk, P. Agostini, L. F. DiMaura, and D. A. Reis, Nat. Phys. **7**, 138 (2011).

[3] O. Schubert, M. Hohenleutner, F. Langer, B. Urbanek, C. Lange, U. Huttner, D. Golde, T. Meier, M. Kira, S. W. Koch, and R. Huber, Nat. Photonics **8**, 119 (2014).

[4] A. Schiffrin, T. Paasch-Colberg, N. Karpowicz, V. Apalkov, D. Gerster, S. Mühlbrandt, M. Korbman, J. Reichert, M. Schultze, S. Holzner, J. V. Barth, R. Kienberger, R. Ernstorfer, V. S. Yakovlev, M. I. Stockman, and F. Krausz, Nature (London) **493**, 70 (2013).

[5] T. Paasch-Colberg, A. Schiffrin, N. Karpowicz, S. Kruchinin, Ö. Saglam, S. Keiber, O. Razskazovskaya, S. Mühlbrandt, A. Alnaser, M. Kübel, V. Apalkov, D. Gerster, J Reichert, T. Wittmann, J. V. Barth, M. I. Stockman, R. Ernstorfer, V. S. Yakovlev, R. Kienberger, and F. Krausz, Nat. Photonics **8**, 214 (2014).

[6] S. E. Irvine and A. Y. Elezzabi, Appl. Phys. Lett. **86**, 264102 (2005).

[7] S. E. Irvine and A. Y. Elezzabi, Phys. Rev. A **73**, 013815 (2006).

[8] S. E. Irvine, A. Dechant, and A. Y. Elezzabi, Phys. Rev. Lett. **93**, 184801 (2004).

[9] P. Dombi, S. E. Irvine, P. Rácz, M. Lenner, N. Kroó, G. Farkas, A. Mitrofanov, A. Baltuska, T. Fuji, F. Krausz, and A. Y. Elezzabi, Opt. Express **18**, 24206 (2010).

[10] P. Rácz, S. E. Irvine, M. Lenner, A. Mitrofanov, A. Baltuska, A. Y. Elezzabi, and P. Dombi, Appl. Phys. Lett. **98**, 111116 (2011).

[11] G. Herink, D. R. Solli, M. Gulde, and C. Ropers, Nature (London) **483**, 190 (2012).

[12] P. N. Nagel, J. S. Robinson, B. D. Harteneck, T. Pfeifer, M. J. Abel, J. S. Prell, D. M. Neumark, R. A. Kaindl, and S. R. Leone, Chem. Phys. **414**, 106 (2013).

[13] P. Dombi, A. Hörl, P. Rácz, I. Marton, A. Trügler, J. R. Krenn, and U. Hohenester, Nano Lett. **13**, 674 (2013).

[14] Z. Han and S. I. Bozhevolnyi, Rep. Prog. Phys. **76**, 016402 (2013).

[15] R. Soref, IEEE J. Sel. Top. Quantum Electron. **12**, 1678 (2006).

[16] S. Sederberg, V. Van, and A. Y. Elezzabi, Appl. Phys. Lett. **96**, 121101 (2010).

[17] A. R. Motamedi, A. H. Nejadmalayeri, A. Khilo, F. X. Kärtner, and E. I. Ippen, Opt. Express **20**, 4085 (2012).

[18] P. Norton, T. Braggins, and H. Levinstein, Phys. Rev. B **8**, 5632 (1973).

[19] R. N. Dexter, H. J. Zeigler, and B. Lax, Phys. Rev. **104**, 637 (1956).

[20] C. Canali, G. Majni, R. Minder, and G. Ottaviani, IEEE Trans. Electron Devices **22**, 1045 (1975).

[21] Lumerical Solutions, Inc., http://www.lumerical.com/tcad-products/fdtd/.

[22] R. Dekker, N. Usechak, M. Först, and A. Driessen, J. Phys. D **40**, R249 (2007).

[23] P. A. Wolff, Phys. Rev. **95**, 1415 (1954).

[24] R. Newman, Phys. Rev. **100**, 700 (1955).

[25] A. Toriumi, M. Yoshimi, M. Iwase, Y. Akiyama, and K. Taniguchi, IEEE Trans. Electron Devices **34**, 1501 (1987).

[26] E. S. Snow, S. W. Kirchoefer, P. M. Campbell, and O. J. Glembocki, Appl. Phys. Lett. **54**, 2124 (1989).

[27] M. Lippitz, M. A. van Dijk, and M. Orrit, Nano Lett. **5**, 799 (2005).

[28] N. Akil, S. E. Kerns, D. V. Kerns, Jr., A. Hoffman, and J.-P. Charles, IEEE Trans. Electron Devices **46**, 1022 (1999).

[29] See Supplemental Material at http://link.aps.org/supplemental/10.1103/PhysRevLett.113.167401, which includes Refs. [30–49], for descriptions of the numerical modeling and analysis, nanofabrication processing, and additional experimental results.

[30] A. G. Chynoweth and K. G. McKay, Phys. Rev. **102**, 369 (1956).

[31] J. A. Burton, Phys. Rev. **108**, 1342 (1957).

[32] A. G. Chynoweth and G. L. Pearson, J. Appl. Phys. **29**, 1103 (1958).

[33] M. Kikuchi and K. Tachikawa, J. Phys. Soc. Jpn. **15**, 835 (1960).

[34] M. Kikuchi, J. Phys. Soc. Jpn. **15**, 1822 (1960).

[35] R. P. Gupta, W. S. Khokle, H. Adachi, and H. L. Hartnagel, J. Phys. D **14**, L31 (1981).

[36] D. K. Gautam, W. S. Khokle, and K. B. Garg, Solid State Electron. **31**, 1119 (1988).

[37] D. K. Gautam, W. S. Khokle, and K. B. Garg, Solid State Electron. **31**, 219 (1988).

[38] B. M. Arora and N. C. Das, Appl. Phys. Lett. **56**, 1152 (1990).

[39] B. P. van Drieënhuizen and R. F. Wolffenbuttel, Sens. Actuators A **31**, 229 (1992).

[40] J. Bude, N. Sano, and A. Yoshii, Phys. Rev. B **45**, 5848 (1992).

[41] S. Yamada and M. Kitao, Jpn. J. Appl. Phys. **32**, 4555 (1993).

[42] J. Kramer, P. Seitz, E. F. Steigmeir, H. Auderset, and B. Delley, Sens. Actuators A **37–38**, 527 (1993).

[43] A. L. Lacaita, F. Zappa, S. Bigliardi, and M. Manfredi, IEEE Trans. Electron Devices **40**, 577 (1993).

[44] A. T. Obeidat, Z. Kalayjian, A. G. Andreou, and J. B. Khurgin, Appl. Phys. Lett. **70**, 470 (1997).

[45] N. Akil, S. E. Kerns, D. V. Kerns, A. Hoffman,, and J.-P. Charles, Appl. Phys. Lett. **73**, 871 (1998).

[46] M. de la Bardonnie, D. Jiang, S. E. Kerns, D. V. Kerns, P. Mialhe, J.-P. Charles, and A. Hoffman, IEEE Trans. Electron Devices **46**, 1234 (1999).

[47] V. E. Houtsma, J. Holleman, N. Akil, L. M. Phoung, V. Zieren, A. van den Berg, H. Wallinga, and P. H. Woerlee, in *Proceedings of the CAS, Sinaia, Romania, 1999*, Vol. 2 (IEEE, Piscataway, NJ, 1999), p. 461.

[48] A. T. Fiory and N. M. Ravindra, J. Electron. Mater. **32**, 1043 (2003).

[49] E. D. Palik, *Handbook of Optical Constants of Solids* (Academic Press, San Diego, 1998).

[50] Q.-Q. Wang, J.-B. Han, D.-L. Guo, S. Xiao, Y.-B. Han, H.-M. Gong, and X.-W. Zou, Nano Lett. **7**, 723 (2007).

[51] S. Sederberg and A. Y. Elezzabi, ACS Photonics **1**, 576 (2014).

[52] F. E. Doany, D. Grischkowsky, and C. C. Chi, Appl. Phys. Lett. **50**, 460 (1987).

[53] A. C. Turner-Foster, M. A. Foster, J. S. Levy, C. B. Poitras, R. Salem, A. L. Gaeta, and M. Lipson, Opt. Express **18**, 3582 (2010).